IOP Publishing Physics in Medicine and Biology

Phys. Med. Biol. **58** (2013) 5009–5028 doi:10.1088/0031-9155/58/15/5009

Quantification of fibrosis in infarcted swine hearts by *ex vivo* late gadolinium-enhancement and diffusion-weighted MRI methods

Mihaela Pop[1,2,5], Nilesh R Ghugre[1,2], Venkat Ramanan[2], Lily Morikawa[3], Greg Stanisz[1,2], Alexander J Dick[4] and Graham A Wright[1,2]

[1] Department of Medical Biophysics, University of Toronto, Canada
[2] Physical Sciences Platform, Imaging Research, Sunnybrook Research Institute, Toronto, Canada
[3] Pathology Core Centre for Modeling Human Disease, Centre for Phenogenomics, Toronto, Canada
[4] Division of Cardiology, University of Ottawa Heart Institute, Ottawa, Canada

E-mail: mihaela.pop@utoronto.ca

Received 11 February 2013, in final form 30 April 2013
Published 8 July 2013
Online at stacks.iop.org/PMB/58/5009

Abstract

Many have speculated that MRI signal characteristics can be used to identify regions of heterogeneous infarct associated with an arrhythmogenic substrate; however, direct evidence of this relationship is limited. The aim of this study was to demonstrate the remodelling characteristics of fibrosis by means of histology and high-resolution MR imaging. For this purpose, we performed whole-mount histology in heart samples ($n = 9$) collected from five swine at six weeks post-infarction and compared the extent of fibrosis in the infarcted areas delineated in these histological images with that obtained *ex vivo* by MRI using late gadolinium-enhancement (LGE) and diffusion-weighted imaging (DWI) methods. All MR images were obtained at a submillimetre resolution (i.e., voxel size of $0.6 \times 0.6 \times 1.2$ mm^3). Specifically, in the histology images, we differentiated moderate fibrosis (consisting of a mixture of viable and non-viable myocytes, known as *border zone*, BZ) from severe fibrosis (i.e., the dense scar). Correspondingly, tissue heterogeneities in the MR images were categorized by a Gaussian mixture model into healthy, BZ and scar. Our results showed that (a) both MRI methods were capable of qualitatively distinguishing *sharp edges* between dense scar and healthy tissue from regions of *heterogeneous* BZ; (b) the BZ and dense scar areas had intermediate-to-high increased values of signal intensity in the LGE images and of apparent diffusion coefficient in the DWI, respectively. In addition, as demonstrated by the Picrosirius Red and immunohistochemistry stains, the viable bundles in the BZ were clearly separated by thin collagen strands and had reduced expression

[5] Author to whom any correspondence should be addressed.

of Cx43, whereas the core scar was composed of dense fibrosis. A quantitative analysis demonstrated that the comparison between BZ/scar extent in LGE and DWI to the corresponding areas identified in histology yielded very good correlations (i.e., for the scar identified by LGE, R^2 was 0.96 compared to $R^2 = 0.93$ for the scar identified in ADC maps, whereas the BZ had $R^2 = 0.95$ for the correlation between LGE and histology compared to $R^2 = 0.91$ obtained for ADC). This novel study represents an intermediate step in translating such research to the *in vivo* stages, as well as in establishing the best and most accurate MR method to help identify arrhythmia substrate in patients with structural heart disease.

(Some figures may appear in colour only in the online journal)

1. Introduction

Heart disease is a major leading cause of death in the industrialized world, with myocardial infarction having the highest prevalence (i.e., >85%) and accounting annually for almost half a million deaths in North America (Zipes 2005). Following an acute infarction, collagen (i.e., the main component of cardiac connective tissue that forms a supportive extracellular matrix in the heart) (McCormick and Thomas 1998, Young *et al* 1998) deposition is part of a prolonged ventricular remodelling process (Fishnein *et al* 1978, Swynghedauw 1999, Rouillard and Holmes 2012). There is early experimental evidence that by approximately four weeks after the insult, mature fibrosis has replaced necrotic myocytes and the myocardial architecture is significantly altered in the scar (McCormick *et al* 1994, Holmes *et al* 1994, Axel 2009). The deposition of fibrosis is due to a continuous collagen turnover, a degradation that is a key feature in characterizing hearts with structural damage of ischemic origin (Sun and Weber 2005, de Backker *et al* 1990, Fomovsky and Holmes 2010). However, this remodelling process is often heterogeneous in nature due to surviving blood vessels which continue to supply oxygen to islands of cells. These viable but ischemic myocytes, together with small patches of necrotic cells, can be either found at the periphery of the scar, referred to as peri-infarct or traversing the dense scars, and form the so-called *border zone*, BZ (Ursell *et al* 1985). As a consequence of having an altered structure and electrical properties, the BZ forms the *substrate* for abnormal and potentially lethal arrhythmias in patients with prior infarction (Kawara *et al* 2001). Thus, accurate identification of BZ and subsequent substrate ablation has been a primary goal of electrophysiology (EP) studies in recent decades (Gardner *et al* 1985, Stevenson 2009). However, despite remarkable technological advances, the typical clinical evaluation of patients with prior infarction in the EP laboratory is still based on invasive catheterizations (with most procedures involving ionizing radiation) and is limited to surfacic maps of sparsely located cardiac electrical signals (Arenal *et al* 2003, Stevenson *et al* 2008). Therefore, the EP study often fails to identify the substrate deep in the myocardium and to provide an accurate diagnostic assessment and/or determination of the best therapeutic approach.

These limitations have triggered pre-clinical and clinical research efforts to develop and establish novel non-invasive imaging tools that could supplement the information given by EP studies. In particular, image-based myocardial tissue characterization with respect to the *transmural* identification of the infarct has received considerable attention. Several pre-clinical and clinical feasibility studies that used MRI, PET, SPECT and CT have not only demonstrated a relatively good correspondence between the sub-endocardial scar delineated in the tomographic images and those identified in the electro-anatomic maps during EP

studies, but also provided information regarding the transmural extent of the potentially arrhythmogenic substrate (Codreanu *et al* 2008, Dickfeld *et al* 2008, Tian *et al* 2010). Among them, MRI remains the preferred imaging modality routinely used in the clinics (Axel 2002) due to its exquisite capabilities (i.e., excellent tissue contrast, no exposure to ionizing radiation, anatomical information, either 3D imaging or select imaging planes) that lead to superior results in both diagnostic assessment and treatment guidance relevant to the EP studies (Wijnmaalen *et al* 2011). Currently, the clinical gold-standard MR evaluation of myocardial viability in patients with prior infarction is based on contrast-enhancement methods (Mahrholdt *et al* 2002, Chan *et al* 2008, Roes *et al* 2009, Breton *et al* 2011). In the resulting MR images, the scar appears hyperintense because the contrast agent (c.a.) molecules in paramagnetic gadolinium-based agents increase the T1 relaxation rate in the fibrotic area relative to healthy tissue (Lima *et al* 1995, Ramani *et al* 1998, Axel 1998, Young *et al* 2006). This method known as *late gadolinium enhancement* (LGE) is routinely used in the clinics. The most used c.a. is gadopentate dimeglumine which is proved to be safe; however, there is still some safety concern regarding the effect of gadodiamine in patients diagnosed with nephrogenic systemic fibrosis (Marckmann *et al* 2006). Although the peak concentration of c.a. within the infarct areas appears to be at $\sim$15 min (nominal time) after c.a. injection, the concentration of c.a. does not remain constant over a long period of time. Thus, by the time the entire infarct volume is scanned, there might be significant variations in the signal intensity (SI), and this could under-estimate the infarct extent. Alternatively, one can use non-contrast MR methods, like the *diffusion-weighted imaging* (DWI) (Thomas *et al* 2000, Le Bihan 2007). From the DW images, one can calculate *apparent diffusion coefficient* (ADC) parametric maps (see section 2.3 for more details and associated equation) and use them for differential diagnosis purposes. Despite that DWI is a very well-established method used in the clinics to successfully delineate ischemic areas in the infarcted brain (Sotak 2002) and to assess liver fibrosis (Sandrasegaran *et al* 2009), cardiac DWI has received less attention due to its low spatial resolution, artefacts due to motion and long-time scans. Several cardiac studies demonstrated that ADC maps can provide *in vivo* localization of scars in patients with prior infarction (Wu *et al* 2009) and are suitable to characterize *ex vivo*, structural changes in the myocardial tissue at different time points in the healing process (i.e., from acute settings of ischemia to mature chronic fibrosis) (Wu *et al* 2007).

MR image analysis studies have also provided several tissue classification algorithms; however, these methods have led to different results and could either under- or over-estimate the infarction area. For example, several pre-clinical and clinical LGE viability studies used simple methods based on standard deviation (SD) and/or full-width at half-maximum (FWHM) of the SI and categorized tissue into healthy, BZ and dense scar (Bello *et al* 2005, Ashikaga *et al* 2007). While both methods are clinically accepted, other recent methods like the Gaussian mixture models (GMMs) have demonstrated superiority in delineating myocardial infarct areas (Lu *et al* 2010, Hennemuth *et al* 2013). The GMM (just like the spatial maps obtained using fuzzy-logic classification algorithms) is more robust and superior because the user does not have to rely on a random region of interest (ROI) drawn on the remote (healthy) myocardium. The location of such manually delineated ROI is known to impact both FWHM and SD (standards deviation) methods because the SI is not uniform in the remote wall; thus, in particular, the classification of BZ becomes prone to errors. Moreover, for FWHM/SD methods, the BZ is obtained given some user-defined thresholds between the selected remote (healthy) area and the dense scar, and currently there is no final consensus between groups regarding these thresholds. However, regardless of the classification method proposed, there are no MR imaging studies that validate quantitatively the extent of the BZ versus dense scar in large animal models by using whole-mount histopathology and thresholds based on the

severity of collagenous fibrosis, as acknowledged by Schelbert *et al* (2010). Moreover, there has been no quantitative comparison to date between tissue heterogeneity (i.e., BZ versus dense scars areas) delineated by LGE versus DWI imaging methods. Finally, *in vivo* clinical studies routinely use slice thicknesses of 8–10 mm in both types of images LGE and DW (Bello *et al* 2005, Wu *et al* 2009), which results in inaccurate discrimination of BZ versus dense scar due to the significant partial volume effect within voxels, as demonstrated by Schuleri *et al* (2012). Thus, an accurate MR-histology validation study should be first performed at high-spatial resolution, preferably *ex vivo* where perfusion and motion do not produce artefacts that can affect image quality and subsequent tissue classification.

The work presented in this paper addresses some of these issues, with a final aim to provide valuable insights into the structural characteristics of potentially arrhythmogenic substrates. Specifically, we sought to better understand by means of MR imaging and histopathology, the morphological characteristics of the dense fibrotic scar as well as of the ischemic BZ, using a pre-clinical swine model of chronic infarction (relevant to the human heart). Specifically, this paper's main objectives are as follows: (1) to generate parametric maps of fibrosis (i.e., BZ and dense scar) from high-resolution LGE and DWI, along with the validation of tissue categorization against histology; (2) to determine if there is a significant difference between the extent of the BZ and dense scars as identified by LGE versus DWI methods. To achieve this, we performed (a) a classification of myocardial tissue into three categories (healthy, BZ and dense scar) using the GMM method; (b) a quantitative validation of MR-based tissue classification against histopathology based on the extent of collagenous fibrosis identified with a Picrosirius Red stain. To the best of our knowledge, such a study including a histological validation as well as a quantitative comparison between LGE and DWI studies has not been performed. This pre-clinical study represents an intermediate step that could be used in the future to relate the MR signal of heterogeneous fibrosis obtained *ex vivo* with that *in vivo*, to optimize *in vivo* experiments and help with the MR data interpretation.

2. Materials and methods

In this section, we describe all experimental details regarding the creation of infarction in the *in vivo* pre-clinical swine model, the preparation of explanted heart phantoms, the MR image acquisition and analysis, as well as the histological studies and associated statistical analysis.

2.1. Animal model preparation and myocardial infarction generation

In this work, we used five juvenile Yorkshire swines weighing 20–25 kg, supplied by the University of Guelph (Ontario, Canada). Myocardial infarction was induced in these swine percutaneously. All procedures were conducted in accordance with protocols approved by the Animal Care Committee of Sunnybrook Health Sciences Centre (Toronto). The animals were sedated with an anaesthetic based on a mixture of ketamine (30 mg kg^{-1}) and atropine (0.05 mg kg^{-1}). The animals were then intubated and the respiration was controlled during the procedure with a mechanical ventilator and inhalation of isoflurane (1–5%). In addition, an intravenous line was inserted via the ear vein for the administration of anti-arrhythmic drugs during the infarct generation (i.e., 30 ml of 2% lidocaine in 250 ml saline and 50 mg amiodarone were administered IV). Briefly, the procedures involved the occlusion of either the left anterior descendant artery, LAD ($n = 3$ animals) or the left circumflex artery, LCX ($n = 2$ animals) for 90 min, followed by reperfusion. All procedures were guided via x-ray fluoroscopy (OEC 9800, GE Healthcare, Milwaukee, WI, USA). Iodine-based angiographic contrast was used to guide the catheterization procedure (i.e., the balloon placement and

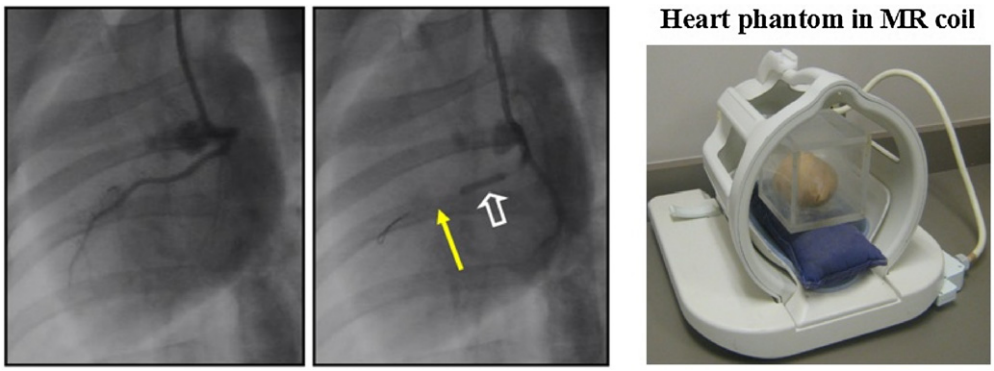

(a) (b) (c)

Figure 1. Typical angiographycally guided generation of myocardial infarction and the heart phantom prepared for the MR scan: (a) and (b) fluoroscopic views taken during the generation of myocardial infarction in the swine model, during the occlusion–reperfusion procedure: (a) iodine contrast entering the LAD; (b) the occluding balloon (indicated by the solid arrow) inflated in LAD produced cessation of the blood flow (indicated by the open arrow); (c) snapshot of the heart phantom placed in the high-resolution eight-channel brain coil, prior to MR imaging study.

inflation inside a main artery or a major arterial branch, as well as the verification of coronary blood flow abnormalities), as shown in figure 1. Figure 1(a) shows an exemplary fluoroscopic view of a swine heart during the iodine injection into the LAD, prior to the insertion of the occluding catheter. Figure 1(b) demonstrates that the coronary blood flow is blocked (solid arrow) in the LAD territory following the inflation of the balloon catheter (Sprinter Legend Balloon Catheter, Medtronic, MN, USA). Reperfusion was established after 90 min by balloon deflation and retraction from the artery, with reperfusion verified angiographically. The lesions were then allowed to heal over a period of 5–6 weeks prior to imaging. We opted to use this occlusion–reperfusion model based on several recent MR-EP studies which were able to create heterogeneous infarctions with a similar model and showed good correspondence between the location of the BZ in MR images and the location of arrhythmia substrate in associated EP studies (Ashikaga *et al* 2007).

2.2. Heart explantation and MR phantom preparation

For the imaging studies, a bolus of 0.2 mmol kg^{-1} Gd-DTPA (gadolinium–diethyleneriamine–pentacetate, an extracellular extra-vascular MR c.a.) was injected intravenously in each animal 15 min prior sacrifice. Imaging 15 min after contrast injection is a standard clinical time point used in myocardial viability studies based on Gd-chelates, allowing the c.a. to slowly accumulate through passive diffusion into the infarcted area; by this time, the agent has been substantially flushed out from the extracellular space and the capillary bed of the healthy tissue (Kim *et al* 1999). Prior to euthanasia, 2000 units of heparin were injected to avoid blood clotting after the explantation of the heart.

Following animal sacrifice, each heart was excised, quickly washed with saline and gently stuffed (with a soft fabric) to preserve heart's shape. To avoid potential susceptibility artefacts at the heart–air interface, each heart was placed in a Plexiglas phantom box filled with Fluorinert (electronic liquid, 3M^{TM}, USA), an inert, transparent fluid that has no MR signal. The phantom was then placed in a high-resolution eight-channel brain coil (figure 1(c)), and the MR study was performed. The phantom preparation was completed within 40–45 min

from the euthanasia time point, allowing any sporadic post-mortem twitching to disappear. Note that each heart was placed on its 'posterior side' onto the bottom of the phantom, and with the heart's longitudinal axis aligned parallel with the direction of the static magnetic field in the MR scanner.

We first imaged the hearts using the LGE method (see section 2.3 for MR imaging parameters). Then, each heart was gently removed from the phantom, fixed in 10% formalin for approximately —three to four days, replaced in the phantom and re-imaged using the DWI methods. We minimized as much as possible the heart deformation between the two MR imaging studies. The minimal heart deformation was ensured between the MR scans by suspending the heart in the vertical position in a jar for 3–4 days fixation in formalin (after which the heart was hardened, and no deformations were likely to occur).

2.3. High-resolution LGE and DW-MR imaging

All MRI studies were performed on a dedicated 1.5T GE Signa Excite scanner. The LGE study (including the localizers and test scans) were completed in less than 2 h after the heart's explantation. That timing was to avoid MR contrast reduction associated with the Gd-based c.a. passively diffusing from the infarcted area into the healthy myocardium beyond a 2–3 h window, as suggested by other animal studies (Rehwald *et al* 2002, Schelbert *et al* 2010).

For this contrast-enhanced MR imaging study, we applied a 3D Inversion Recovery Gradient Echo, IR-GRE sequence with the following MR parameters: repetition time TR = 5.98 ms; echo time, TE = 2.8 ms; inversion time TI = 200 ms (manually adjusted to optimally null the myocardium); echo train length = 1, flip angle = 25°. Other imaging parameters were field of view, FOV = 16 × 16 cm, *k*-space 256 × 256, slice thickness 1.2 mm, yielding an approximately 0.625 mm × 0.625 mm in-plane spatial resolution and a voxel volume of ∼0.47 mm^3. No phase-sensitive inversion recovery was used.

For the DWI, we used a custom FSE pulse sequence that was developed by the Laboratory of Cardiac Energetics, NIH (Helm *et al* 2005) and implemented on our 1.5T GE Signa Excite scanner, as previously described (Pop *et al* 2012). To avoid susceptibility artefacts, we did not combine the sequence with any echo-planar, parallel imaging or sensitivity encoding methods. In the current study, we used the following MR parameters: TE = 35 ms, TR = 700 ms, echo train length = 2; *b* value = 0 for the un-weighted MR images and $b = 500$ mm s^2 when the seven diffusion gradients were applied, respectively. We used the same FOV and a 256 × 256 *k*-space (yielding an identical in-plane spatial resolution and slice thickness as in the LGE studies). The total scan time for DW imaging was approximately ∼10 h (depending on the heart size); for this reason, more *b*-value scans were not performed. The DW images were then imported into the freely available software DTIstudio (Jiang *et al* 2006), which was used to evaluate ADC parametric maps. Fitting using multiple *b* values could have improved the resulting ADC maps and image quality. The calculation of ADC (also known as 'trace' or 'mean diffusivity') was based on the method proposed by Le Bihan and Van Zijl (2002). We should mention in brief that the DWI method was developed based on the 'field gradient pulse' method originally devised for NMR by Stejskal and Tanner (1965) who calculated the attenuation in SI in DW images caused by the amount of diffusion of water molecules. This 'random walk' of water molecules occurs during the application of 'motion-probing' pulses, such that, at the echo time, a measurable 'phase accrual' is accumulated for the proton spins within each voxel. However, such a calculation is quite complex because cross-terms arise between all gradient pulses and the intensity of each voxel is in fact exponentially weighted by an average diffusion coefficient (Taylor and Bushell 1985, Mattiello *et al* 1997). Le Bihan (1991) suggested gathering all gradient terms in a diffusion-sensitive '*b* factor' that depends

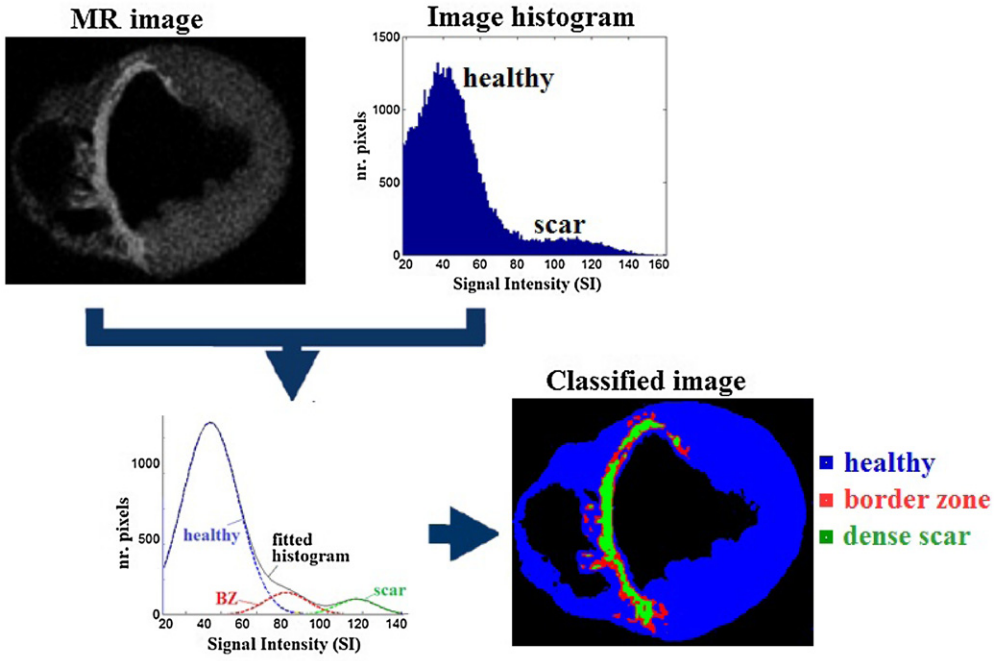

Figure 2. Example of a myocardial tissue classification into three classes (i.e., healthy, BZ and dense scar) from an LGE image using a GMM.

only on the MR acquisition parameters, such that the signal SI attenuation becomes

$$\mathrm{SI} = \mathrm{SI}_0 \times \exp(-b \times \mathrm{ADC}) \tag{1}$$

where SI_0 is the signal intensity of the un-weighted images (i.e., in the absence of diffusion gradients), for which the b factor is 0 s mm^{-2}, and ADC is a physical parameter of biological tissues (such as brain and myocardium).

Finally, the LGE and DW images were registered with the freely available MedINRIA software (www-sop.inria.fr/asclepios/software/MedINRIA).

2.4. Myocardial tissue classification in MR images

In this paper, we characterized the myocardium heterogeneities based on the SI in LGE images and the ADC parametric maps from DW images, respectively. For this, we used a classification method based on a GMM (Press *et al* 2007). Briefly, the GMM assumes a Gaussian distribution of the image intensity of each fitted class (i.e., in our case, the three categories of tissue: healthy, BZ and dense scar), each class having its own mean intensity μ and variance σ^2. The GMM code generated the tissue classification that optimally fitted the image histogram, where the GMM was estimated by employing an expectation–maximization approach (Dempster *et al* 1977, Hastie *et al* 2001). However, for our tissue segmentation purposes, we used and adapted the freely available Matlab scripts (Mathwork, CA) (http://mathworks.com/matlabcentral/fileexchange/10956-em-image-segmentation/content/EMseg.m). The outcome was the probability of a pixel belonging to a category and its Gaussian description, based on which the final classified image was obtained

by assigning each pixel to its most likely class (see figure 2 for an example where the pixels were assigned to the three categories).

2.5. Histopathology and immunohistochemistry (IHC)

Following the DWI measurements, selected slabs (5 mm thickness) as well as small samples from each heart were cut to align with the short-axis view of MR images, and embedded in paraffin. Prior slicing into slabs, the heart was embedded in a gelatine matrix and a special slice cutter was used, such that no tissue deformation occurred. Thin slices (4 μm) were cut from each paraffin block, fixed on glass slides and then stained. The large specimens were whole-mounted on large slides and were stained with (1) *Haematoxylin and Eosin* for oedema, myocardial fibres integrity, and small blood vessels; and (2) *Picrosirius Red* for the evaluation of collagenous fibrosis. The small specimens were used for IHC and were stained for connexin 43 (Cx43) in order to observe the distribution of gap junctions in the BZ and dense scar compared to that in the remote zones. All stained slides were scanned with a TISSUEscope^{TM} 4000 confocal system (Huron Technologies International Inc.), saved as multi-resolution digital images and analysed with Aperio ImageScope software (Vista, CA) at a 10–15 $\times$ magnification (of original scan). In the absence of a standardized classification system to grade the myocardial fibrosis in chronic infarct, in this paper, we defined three grades of fibrosis for the three tissue types: F0 ($<$20% fibrosis, *no or mild*) for normal/healthy tissue, F1 (20–70% fibrosis, *moderate*) for BZ and F2 ($\geqslant$70% fibrosis, *severe*) for dense scar. The chronic lesions were manually delineated by an expert, who categorized the infarct areas into two zones: dense scar and BZ, based on scoring the fibrosis severity as F2 and F1, respectively. For the F0 grade, we considered the tissue as 'normal/healthy', although (1) the interstitial (reactive) fibrosis in the remote ventricular areas distal from the scar was increased at this healing stage (i.e., 5–6 weeks), and (2) extracellular space was also increased in the remote myocardium. These two observations are based on findings by our group in a recent longitudinal study (Ghugre *et al* 2011). Both the BZ and the dense scar demonstrated interstitial and replacement fibrosis, with red areas in the PR stain positively indicating fibrotic material (mainly type-3 collagen degraded into type-1 collagen) and perivascular collagen, which was also included in the infarcted areas due to the comparison with the MR images. Thus, when scoring the fibrosis severity and tracing the contours of these two zones, both replacement and reactive fibrosis, other fibrotic material (fragments of disintegrated dead myocytes, perimysial coils and pericellular weaves with altered morphology) as well as extracellular space (interstitial space and small blood vessels) were all included in the corresponding F1 or F2 areas. For aid in the manual delineation, we used the AperioScope ruler which allowed us to decide on tissue categorization within squares of 0.6×0.6 mm, to match the MRI in-plane resolution. The histological samples (a total of $n = 9$ from the five swine, 1–2 samples/animal) were matched to their corresponding MR images in a short-axis view, using anatomical markers (papillary muscle and RV/LV insertion point).

2.6. Statistical analysis

The results were expressed as mean $\pm$ SD (standard deviation) for ADC values and SI (in LGE). Linear fittings and Bland–Altman plots (Bland and Altman 1986) were performed in Excel and Matlab to calculate the correlation between the extent of BZ and dense scar categorized in MR images (LGE and DW) and in histopathological images, respectively. Statistical significance tests were performed with an on-line calculator (www.vassarstats.net), where p-values <0.05 were considered statistically significant.

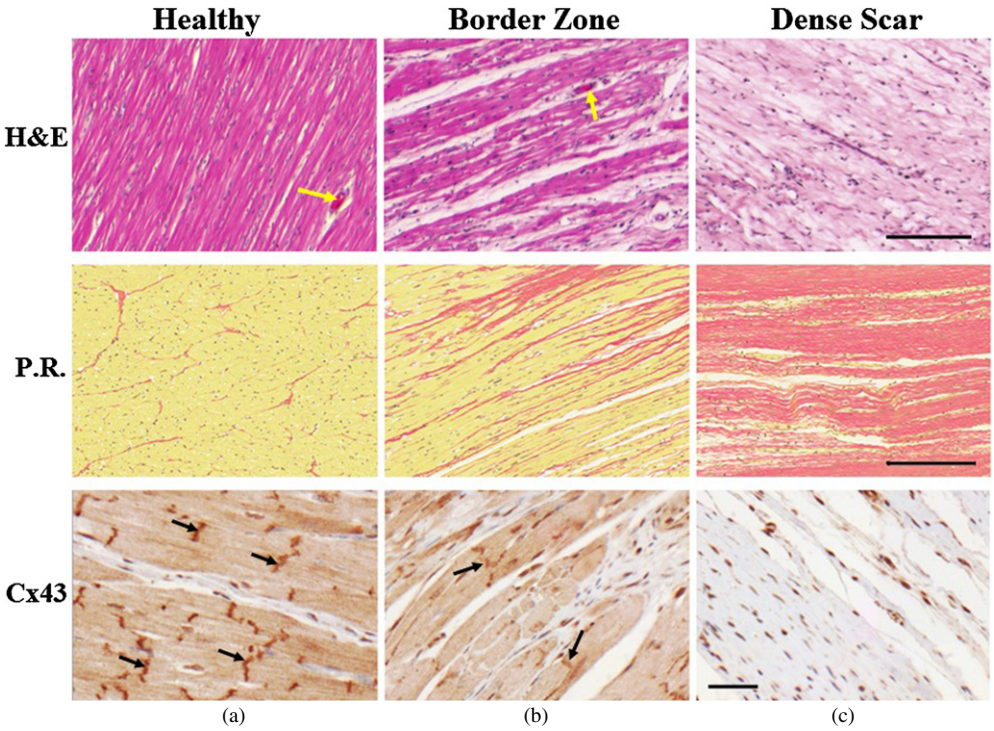

Figure 3. Representative images from histopathology (Haematoxylin and Eosin, Picrosirius Red) and IHC (for connexin Cx43), from a swine heart with a six-week-old infarction: (a) healthy myocardium (fibrosis severity extent $\leqslant 20\%$), score F0; (b) typical patchy fibrosis in the ischemic BZ (fibrosis score between 20% to 70%) graded F1; and (c) dense scar with collagenous fibrosis extent $\geqslant 70\%$ (score F2), with myocytes staining in yellow and collagenous fibrosis in red (see text for more details). In the H&E images, the yellow arrows indicate small blood vessels (in the healthy tissue and the BZ), whereas in the IHC images, the black arrows indicate the Cx43 clustered at the intercalated disks of myocytes (note: the images show the longitudinal direction of cells). The scale bar is 200 μm in the H&E and P R stains, and 50 μm in the Cx43 images, respectively.

3. Results

The creation of heterogeneous infarction was confirmed by histopathology, in all animals. Figure 3(a) shows intact myocytes in the normal tissue, whereas figures 3(b) and (c) demonstrate the changes in the tissue microstructure in the infarcted area. As depicted by the H&E stain (upper images) and the P R stain (middle images), the ischemic BZ of the infarct had strands of fibrosis interdigitated between viable bundles of myocytes (figure 3(b)). In the dense scar area, necrotic myocytes were replaced by mature fibrosis, the final product of collagen degradation (figure 3(c)).

Histopathology using the H&E stain confirmed that oedema subsided substantially 5–6 weeks after infarction and that the inflammation had largely disappeared by this time point in wound healing. Relatively small blood vessels were always noted in the viable tissue (healthy and BZ); however, a few surviving large vessels were also identified inside the dense scars. Surviving islands of viable myocytes mixed with collagenous cells were observed in all animals, and were mostly located at the periphery of infarct and were likely salvaged by the reperfusion. Surviving sub-endocardial bundles were often noted, but their viability was

Table 1. MR characteristics and histological grades of fibrosis in chronic infarct swine corresponding to healthy tissue, BZ and dense scar.

Tissue category	Absolute ADC values ($\times 10^{-3}$ mm^2 s^{-3}) (mean $\pm$ SD)	Normalized SI (LGE) (mean $\pm$ SD)	Fibrosis grade
Healthy	0.62 $\pm$ 0.10	1	F0 (no or mild) fibrosis $\leqslant$20%
Border zone	0.84 $\pm$ 0.13	1.53 $\pm$ 0.27	F1 (moderate); between 20% and 70%
Dense scar	1.12 $\pm$ 0.19	2.16 $\pm$ 0.38	F2 (severe); fibrosis $\geqslant$70%

probably due to the oxygen molecules diffusing from the blood in the adjacent left ventricle (LV) cavity into the sub-endocardial tissue. Also, as confirmed by both H&E and P R stains in all animals, there was an increased extracellular space in both BZ and dense scar areas, supporting similar qualitative MRI-based observations, as presented below. Hypertrophy of the LV was observed in two out of six animals, in which the infarction was generated in the LAD territory and the chronic lesion extended throughout the entire septum. Other remodelling characteristics as pertaining to the myocardial architecture included gradual disarray of fibres in the BZ and severe loss of anisotropy (i.e., fibre direction) in the dense scar area.

IHC (bottom images in figure 3) demonstrated a reduced expression of Cx43 with an altered distribution of gap junctions in the viable myocytes of the BZ compared to their high density and well-organized distribution in the normal cells. It is clearly observable that the Cx43 clusters at the intercalated disks in the BZ had a less intense brown colour compared to those in the healthy areas, as indicated by the black arrows. Fibrotic strands infiltrating between viable bundles were notable in the BZ area, which electrically disconnected the cells. Furthermore, IHC demonstrated that Cx43 largely disappeared in the dense scar area, although in some samples we did observe scattered viable foci with the reduced Cx43 expression, encapsulated inside fibrotic scars. Such areas characterized by the reduced Cx43 content and cellular uncoupling, together with particular geometric configurations of viable bundles surrounded by electrically inert scars, could favour the inducibility of ventricular arrhythmias.

Histopathology also demonstrated that, at 5–6 weeks after infarction, some regions at the periphery between the healthy tissue and the infarct exhibited patchy fibrosis (i.e. tissue having a mixture of viable myocytes and strands of collagen), whereas in other peripheral regions, the scar was sharply delineated from the normal myocardium. Both LGE and DWI methods were able to resolve these fine remodelling features, as confirmed by histopathology (figure 4). Specifically, we highlight in figure 4 an example of heterogeneous BZ (see zone 1, red square) versus a region with a sharp edge (see zone 2, blue square) in the periphery of an antero-septal infarction. In figure 4 (bottom), two magnified PR images of these zones '1' and '2' are also included, with their topographic locations precisely indicated in the LGE and DW-MR images as well as in the histopathology image.

Table 1 shows the mean $\pm$ SD of ADC values and of normalized SI in LGE (note that the SIs were normalized to the healthy SI values), corresponding to the three tissue categories (i.e., fibrosis grades): healthy tissue (F0), BZ (F1) and dense scar (F2), respectively. The mean ADC values were increased by 35% in the BZ and 81% in the dense scar compared to the healthy areas, whereas the SI increased by 53% in the BZ and 116% in the scar, respectively, compared to the remote (healthy) areas in the LGE images.

Figure 5(a) presents a bar plot describing the absolute ADC values (mean and SD) and the normalized SI for LGE (mean and SD), for the three grades of fibrosis. Figure 5(b) shows an example of moderate fibrosis (F1) selected from a PR stain image, at near cellular resolution. The mean ADC values were increased by 35% in the BZ ($p < 0.011$) and 81% in the dense

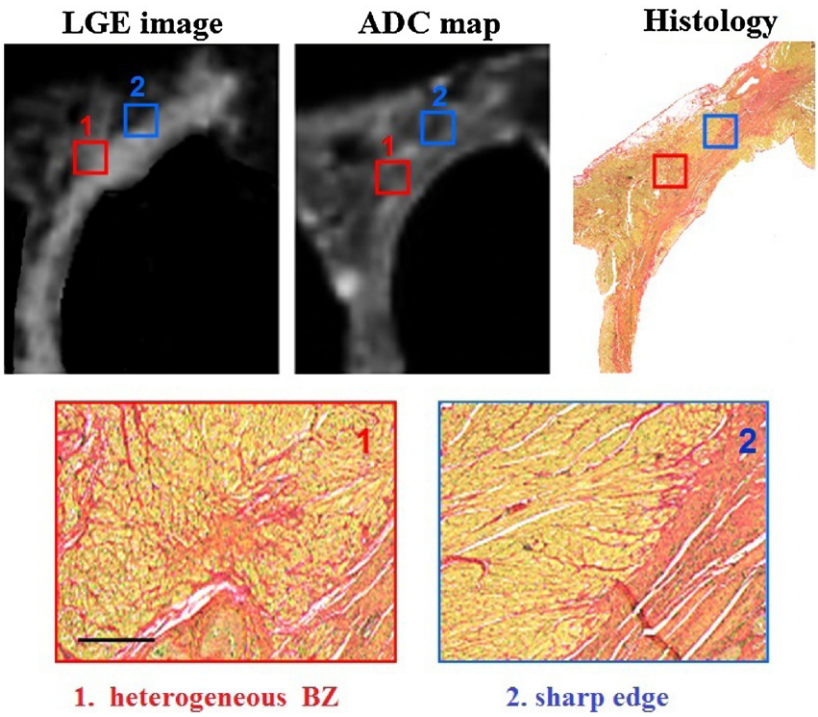

Figure 4. Representative images from *ex vivo* MR studies and histopathology, from an antero-septal chronic lesion, showing the hyper-enhanced infarction area in the LGE image and elevated ADC values in the DW-MR image, as well as the corresponding histopathology image (P R stain). Two magnified zones from the P R stain were selected from zone '1' (red square) heterogeneous BZ due to patchy fibrosis, containing mixture of viable myocytes and collagenous fibres, and '2' (blue square) peri-infarct with sharp edge (i.e., abrupt transition between dense fibrotic scar and normal myocardial tissue, as seen in the blue square). Scale bar 200 μm.

scar ($p < 0.001$) compared to the healthy areas, whereas the SI increased by 53% ($p < 0.02$) in the BZ and 116% in the scar ($p < 0.001$), respectively, compared to the remote (healthy) areas in the LGE images (where $p < 0.05$ was considered statistically significant).

Figure 6 shows a comparison between the MR images (LGE and ADC map) and the corresponding histopathology image (upper images), as well as the result of classification in each of these images (bottom images). The example was selected from a swine with the infarction generated in the LAD territory (apical slice). Overall, a good agreement was observed between the extent of tissue in both MR images classified by the GMM as healthy myocardium (in blue), dense scar (in green) and BZ (in red). Moreover, as seen in the bottom images of figures 6(a) and (b), this classification also corresponded well with the same categorization of tissue delineated in the PR stain image, based on the severity of collagenous fibrosis.

Figures 7 and 8 show results from the quantitative comparison between the areas of scar and BZ (reported relative to LV area) calculated in the segmented LGE and ADC maps, versus those delineated in the histology images. Linear fitting yielded good correlations for the % (scar area/LV area) measured in both types of MR images versus the corresponding scar areas in the PR stain (i.e., $R^2 = 0.96$ for LGE and $R^2 = 0.93$ for the ADC map, respectively) as seen in figures 7(a) and (b), with no bias between the MR and histology demonstrated by the Bland–Altman analysis (figures 7(c) and (d)). The difference was not statistically significant

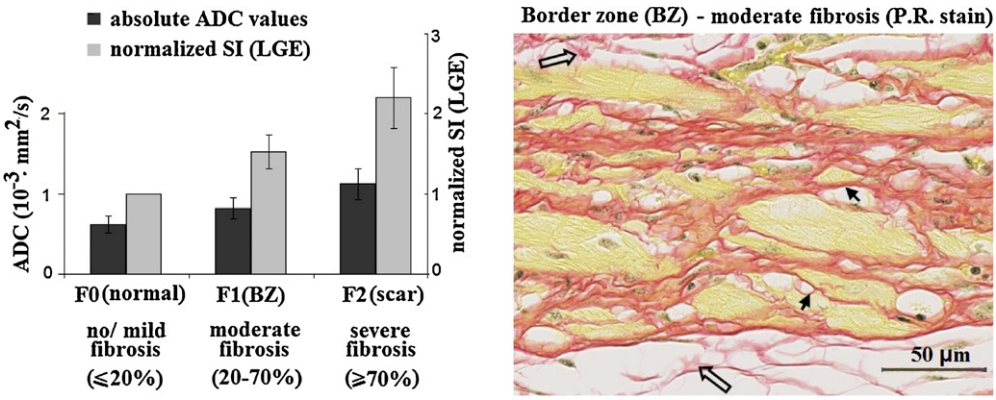

(a) (b)

Figure 5. MR and histological characteristics of fibrosis: (a) bar plot of the average ADC values and normalized SI in LGE, corresponding to healthy, BZ and scar (where tissue categories are based on fibrosis grades); (b) example of F1 from the BZ, with collagen fibrils (red). The increased extracellular space (white) and an increased amount and thickening of other collagen matrix components are also notable, such as the perimysial coils (open arrows) and pericellular weaves (small arrows); scale 50 μm.

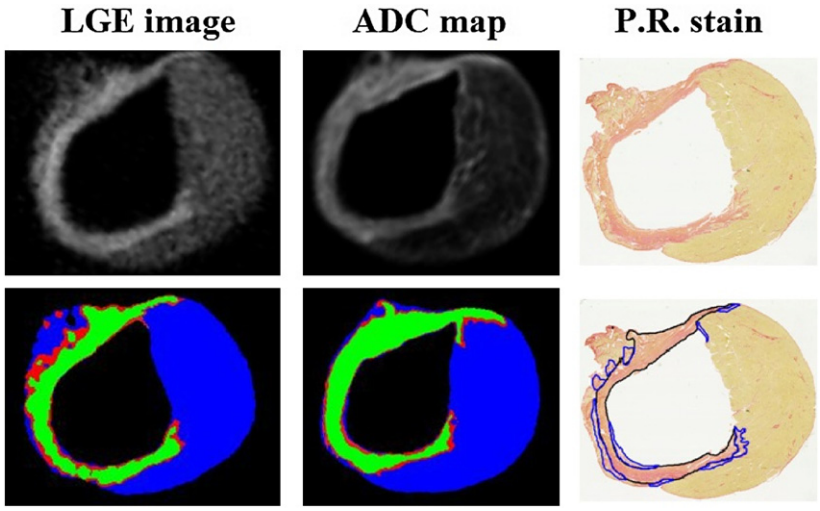

(a) (b) (c)

Figure 6. Example of MR images and histological slides from an animal with an LAD lesion (*upper images*) and corresponding tissue categorization in these slides (*bottom images*): (a) LGE image with infarcted area having a hyper-enhanced signal; (b) ADC parametric map with elevated ADC values in the infarction area; (c) corresponding histological P R stain (fibrosis stained red and normal tissue stained yellow). In the segmented MR images, the scar is green, the BZ is red and the healthy tissue is blue, whereas in the PR stain the scar has a black contour, the BZ has a blue contour, and the remaining tissue is healthy.

by a one-tailed test ($p = 0.3$) between the two MRI methods ($n = 5$), (where $p < 0.05$ was considered statistically significant).

Similarly, a linear fitting yielded good correlations for the % BZ area relative to the LV area identified in MR images versus the corresponding BZ areas delineated in the PR

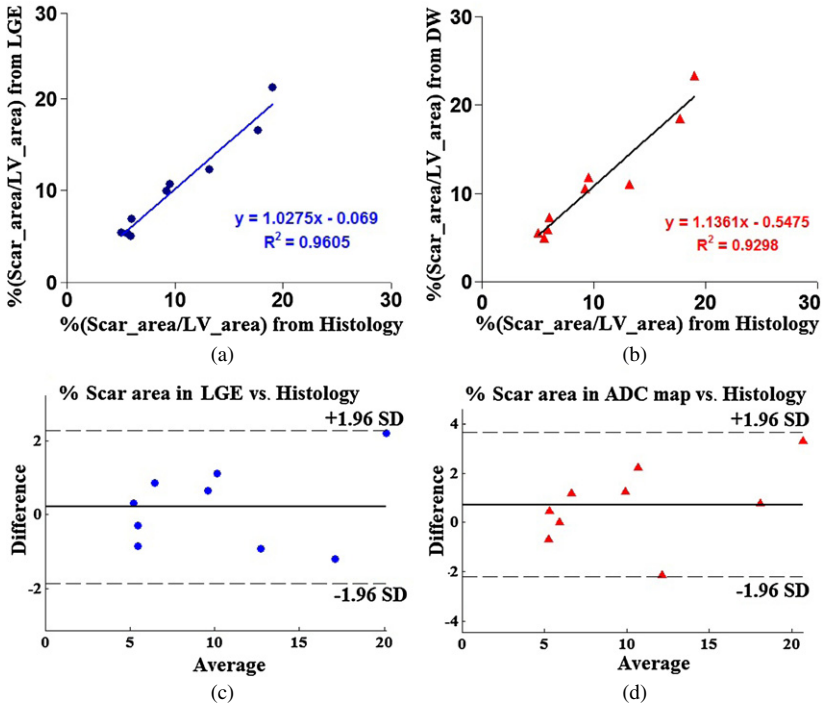

Figure 7. Results of quantitative comparison between MR methods and histology for dense scar: (a) and (b) linear fitting of % (scar area/LV area) identified by LGE (blue circles) and ADC maps 70 (red triangles), respectively, versus those delineated in histological images, yielding very good correlation between the collagen-rich scar identified by both MR methods and by the P R stain ($R^2 = 0.96$ for LGE compared to $R^2 = 0.93$ for ADC; (c) and (d) corresponding Bland–Altman plots.

histological stain. Although a slightly stronger correlation was demonstrated by the LGE ($R^2 = 0.95$) compared to ADC ($R^2 = 0.91$), as seen in figures 8(a) and (b), this was not statistically significant ($p = 0.26$). Furthermore, no bias was noted between the % BZ areas calculated from the segmented images obtained by the two MR methods and histology, as demonstrated by the corresponding Bland–Altman analysis (figures 8(c) and (d)). Overall, we also observed slightly weaker correlations of the % BZ areas (figure 8) compared to the % dense scar areas (figure 7), making the LGE to appear more favourable. This could be due to the quality of the ADC maps which were obtained using only two data points (more b value scans could have improved the ADC maps quality and the classification result).

4. Discussion

MR imaging represents an important tool that can be used in the non-invasive detection of BZ, where the potential arrhythmia substrate resides and is characterized by heterogeneous fibrosis. Overall, the work presented in this paper demonstrated the capability of two different MRI methods (LGE and DW) to distinguish *ex vivo* the BZ and dense collagenous scar within the chronic infarct areas in a swine model, with LGE appearing slightly superior to the diffusion-weighted method when compared to histopathology. The potential mechanisms responsible for these findings together with the study implications and limitations are addressed below.

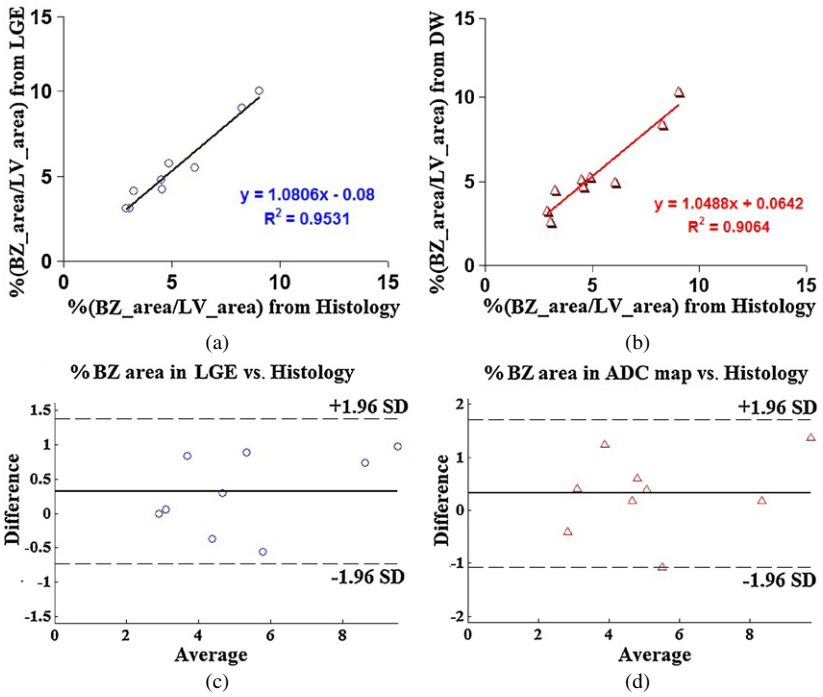

Figure 8. Results of quantitative comparison between MR methods and histology for BZ: (a) and (b) linear fitting of % (BZ area/LV area) identified by LGE (open blue circles) and ADC maps (open red triangles), respectively, versus those delineated in histological images, yielding very good correlation between the BZ identified by both MR methods and by the PR stain ($R^2 = 0.95$ for LGE compared to $R^2 = 0.91$ for ADC; (c) and (d) corresponding Bland–Altman plots.

First, in the histopathology images, several key remodelling characteristics were retained as hallmark signatures of fibrosis and were attributed to the healing phase at 5–6 weeks as well as to the occlusion–reperfusion approach that induced infarction. Among the main histological findings, the mature collagenous fibrosis in the core scar and a mixture of surviving viable bundles (due to reperfusion) and necrotic cells/bundles in the BZ were notable, in agreement with other studies performed in explanted human hearts (de Bakker *et al* 1990, Kawara *et al* 2001), rat hearts (McCormick *et al* 1994, Schelbert *et al* 2010) and pig hearts (Holmes *et al* 1994). Oedema and inflammation had almost disappeared by this point in the healing process compared to that seen in the first days to weeks after ischemic injury, as indicated in our recent longitudinal study (Ghugre *et al* 2011). In particular, the Picrosirius Red stain, which is the most accurate stain used in the quantitative histological analysis of collagen-rich-based scars (Whittaker *et al* 1991) allowed us to grade the severity of fibrosis to correspond to the three distinct tissue categories: healthy (F0), BZ (F1) and dense scar (F2). Although there is a lack of standardized classification systems for myocardial fibrosis, the 20% fibrosis threshold we selected for the healthy zone ('normal' tissue in the remote myocardium) was in agreement with the F0 grade used by Azevedo and colleagues (Azevedo *et al* 2010) in the evaluation of diffuse fibrosis (which is spread globally within the entire ventricle). However, as emphasized in other studies (Schelbert *et al* 2010), currently, there is no histological definition of the BZ versus dense scar for chronic infarction. Thus, in this study, the 70% threshold selected for F1 (BZ) from F2 (dense scar) in the PR stain reflected a significant increase in collagen

deposition, extracellular space, amount of fibrotic debris (from the dispersion of cellular components following the loss of cellular membrane integrity) and perivascular collagen, as well as marked morphological changes for other matrix components (e.g., thickening and increased abundance of perimysial cells and pericellular cells). Importantly, besides the structural changes unveiled by the PR stain, the IHC results showed that moderate fibrosis F1 was also characterized by the reduced Cx43 expression and altered distribution of gap junctions, suggesting that the BZ harbours electrical disturbances and might be a potentially arrhythmogenic substrate. This is in agreement with the electrophysiological findings from Jansen and colleagues (2012) who demonstrated that an increased deposition of reactive and replacement collagen together with a decreased abundance of Cx43 (>50%) leads to cellular uncoupling and decreased conduction velocity (resulting in slowing or complete blockage of the electrical wave propagation).

Regarding MR tissue characteristics, we identified fine structural remodelling features by both LGE and DW imaging methods, which were able to distinguish heterogeneous BZ versus sharp edges (between core scar and healthy myocardium), as well as different fibrosis grades. Specifically, our contrast-based LGE study demonstrated that Gd-DTPA, although not a collagen-specific c.a., was capable of detecting necrosis and fibrosis extent in BZ and dense scar, with the scar extent strongly correlated with that identified by histopathology. The mechanism of the differential enhancement of SI in the infarct area suggested a higher extracellular volume available for the distribution of the Gd molecules within the infarct area compared to the healthy/remote myocardium, affecting the wash-in and wash-out kinetics of Gd in both heterogeneous BZ and dense collagenous fibrosis. Presumably, there was a greater distribution volume and/or slower clearance of the Gd molecules in the dense scar versus BZ, explaining why the SI in LGE images had intermediate values in the BZ (between those measured in the remote tissue and the scar), in accordance with other *ex vivo* and *in vivo* studies evaluating infarct heterogeneities (Bello *et al* 2005, Ashikaga *et al* 2007, Schuleri *et al* 2012). This was also in agreement with the observations of the PR stain images where moderate fibrosis and increased interstitial space characterized the BZ, compared to remote/healthy tissue. Our validation of the extent of BZ and scar against quantitative microscopic histopathology using the PR stain is more accurate than other methods using gross pathology 2,3,5-triphenyl-2H-tetrazolium chloride, which are specific to myocardial viability but not to fibrosis (Kim *et al* 1999, Amado *et al* 2004, Azevedo *et al* 2010). On the other hand, the ADC maps produced slightly weaker correlations of BZ and scar extent versus histology (0.94 and 0.91, respectively), compared to LGE. While these were not statistically significant, it could be that DWI is more sensitive than LGE to the uncompleted disappearance of oedema (at 5–6 weeks) in the infarction since DWI probes a different MR mechanism to discriminate the BZ and scar from healthy areas. In the resulting ADC maps, the detection of collagen-rich fibrotic areas was based on the free diffusion motion of the water molecules along the fibres and in the interstitial (extracellular) space; note that to probe the intracellular space, higher b values are needed, as explained by others (Hsu *et al* 2001). Thus, the molecular diffusion reflected the microstructural tissue integrity in the normal and infarcted areas, with a gradual loss of highly ordered myocardial anisotropy (corresponding to the healthy state) in the ischemic BZ and in the infarct core due to collagen deposition and necrosis. This, together with less cellular obstacles (as the cellular membranes broke and disintegrated), presence of small surviving or newly recruited vessels (i.e., collagenous perivascular space) in the BZ and most importantly a more extracellular space available, explained the increased ADC values in BZ and scar. The ADC values found in our study, ranging from 0.62×10^{-3} mm^2 s^1 (in healthy tissue) to 0.84×10^{-3} mm^2 s^1 (in BZ) and 1.12×10^{-3} mm^2 s^1 (in scar), are comparable to those reported by Wu *et al* (2007) in a similar *ex vivo* DW-MRI porcine study (0.67×10^{-3} mm^2 s^1 in

healthy area and 1.01×10^{-3} mm^2 s^1 in infarcted tissue) using an isotropic voxel size $1.13 \times 1.13 \times 1.13$ mm^3. We expected small differences in ADC values in the infarct area since their 13-week-old non-reperfused infarct was induced by permanent occlusion of blood vessels with microspheres. However, besides they did not perform quantitative comparison MR to histology, their study could not identify intermediate ADC values in the BZ. This could be due to their analysis based on six radial sectors rather than pixel-wise, with 'infarct-adjacent' sectors averaging ADC values of predominantly healthy tissue. In contrast, the *in vivo* results obtained in patients with prior infarction by Wu *et al* (2009) are in closer agreement with our findings and reported increased values in the 'infarct-adjacent' areas (0.74×10^{-3} mm^2 s^1) compared to the remote zones (0.67×10^{-3} mm^2 s^1). Notable though, their ADC values were obtained at a $1.88 \times 1.88 \times 8$ mm^3 voxel size and were averaged per radial segments which could lead to inaccurate values for non-transmural infarctions. The comparison with *in vivo* data has to be done with caution, as fixation procedures could modify ADC values as demonstrated by Shepherd *et al* (2009), Van der Voorn *et al* (2011); however, we kept the samples in formalin for 3–4 days and not for weeks to minimize this effect while targeting the full fixation of the ventricular walls. Moreover, diffusion is a temperature-dependent process, so the difference between the ADC values obtained by us and Wu *et al* (2007), and the *in vivo* values from Wu *et al* (2009) could be partially attributed to this factor, not only to fixation.

Our *ex vivo* MR study shares overall similar MR findings and histological observations with the *ex vivo* study performed in chronically infarcted rat hearts by Schelbert *et al* (2010). Their high correlation (i.e., 96–98%) between the lesion extent in MR and histology was calculated for the total infarction area, without differentiating the BZ versus scar in histological images and without a Cx43 staining. We acknowledge that some caution is needed in comparing our results with their study which was performed at a spatial resolution near the cellular level and demonstrated that the BZ (but not the scar) is sensitive to partial volume effects even at submillimetre resolution. Their conclusion was that at lower resolution (i.e., thicker slices), this difference will be accentuated. Note that we only tested on a few selected images how a poorer spatial resolution affects the categorization, by decreasing the in-plane resolution to $1.2 \times .1.2$ mm^2 (thus obtaining an isotropic voxel) and found that, compared to the higher resolution, the difference in % (scar area/LV area) between higher and poorer resolutions is negligible ($<$1%) for both LGE and DWI, whereas the difference in % (BZ area/LV area) is very small $\sim$1.6% for LGE and 2.1% for DWI. Thus, when decreasing the resolution, more BZ pixels than scar pixels may be misclassified. However, we speculate that when the slice thickness is increased to a few millimetres (as in Schelbert *et al* 2010 or Schuleri *et al* 2012), such differences will be more accentuated due to the partial volume effects. Note that a thorough study concerning the degradation of spatial resolution and its effect on BZ/scar size was not the focus of our current work, but will be certainly performed in the future, particularly when translating this step to *in vivo* studies. Notably, our voxel size was close to the $0.6 \times 0.6 \times 2.5$ mm^3 voxel (interpolated from the initial $1.2 \times 1.2 \times 2.5$ mm^3) recently achieved *in vivo* by a feasibility MR-EP study performed by Cochet *et al* (2013) who reported a 78–94% overlap between the arrhythmogenic substrate determined in LGE and EP studies (i.e., low voltages $<$1.5 mV), underlining the importance of high-spatial resolution in future cardiac MR-EP studies.

To sum up, our study demonstrated that both LGE and DWI performed very well and can distinguish post-infarction focal fibrosis, with the measurement of extent of heterogeneous fibrosis (BZ) and collagen-rich scar in very good agreement with histopathology. One limitation was the use of only one *b*-value scan for the DW imaging, which might affect the image quality and ADC maps. Another limitation of the comparison between the MR and the histology was

that the slice thickness in MR is 1.2 mm, whereas in histology was 4 μm; this could explain the small overestimation of the extent of BZ/scar in the MR images compared to histological measurements. A more accurate comparison should be based on a volumetric analysis of MR and reconstructed histology slabs, but the costs for such histological processing of tissue are currently prohibitive (at least in large mammal hearts). Another limitation was that we did not use fiducial markers for the registration between MR images and histology and relied solely on anatomic markers and distances calculated from the apex upwards (in MR images and histology cuts); however due to unique features and location of the anatomical markers (papillary muscle, RV traebeculations, endocardial/epicardial shapes), we successfully matched all MR images to histology slides. However, as our future will focus on translating this work to *in vivo*, a co-registration method could be the one developed by Young *et al* (2011). Finally, a limitation was the relatively small number of animals (five swines); however, there were nine samples for which whole-mount histology and quantitative analysis were performed, and that proved to be sufficient for the statistical analysis. Experimental chronic infarct studies in animals are extremely difficult and costly to perform; other recent similar MR or MR-EP studies that included histology slides were reported in $n = 6$ rats (Schelbert *et al* 2010), $n = 4$ sheep (Mekkaoui *et al* 2011) and $n = 5$ swine (Nakahara *et al* 2011).

Future work will focus on characterizing post-infarction remodelling using *in vivo* MRI methods, histopathology and EP studies to confirm the relation of BZ and dense scar to actual electrical measurements. In particular, quantitative methods characterizing focal fibrosis based on T1 maps and extracellular matrix volume could lead to more accurate results than IR-GRE in determining the collagen content and the potential arrhythmia substrate.

5. Conclusion

In this work, we demonstrated several remodelling characteristics of chronic infarct in a pre-clinical swine model, with relevance to structural damage from ischemic heart disease in humans. Overall, as determined by two MRI methods (LGE and DWI) and histological analysis, the reperfused infarction had intermediate and severe collagen deposition and increased extracellular space. Specifically, we noted that the BZ was comprised of non-viable and viable bundles separated by thin collagen strands and had reduced cell-to-cell electrical myocyte coupling, whereas the dense scar was composed of mainly collagen and fibrotic material replacing necrotic myocytes. We found that the extent of BZ and fibrotic scar as well as the edge demarcation between healthy tissue and scar can be determined by both MRI methods, and the identification of tissue categories in LGE and DWI led to good correlation compared to histological grades of fibrosis. Our results also confirmed that, although not a collagen-specific contrast-agent, Gd-DTPA can be used with confidence to evaluate the extent of fibrosis in chronic infarction, as well as the remodelling characteristics of the BZ, where the arrhythmia substrate resides.

Acknowledgments

The authors are grateful to Mrs S Newbiggins and Mr Q Xu of Lunenfeld Research Institite, Toronto (CA) for help with histopathology and immunohistochemistry staining and interpretation, to the personnel in the Biomarker Imaging Lab (Sunnybrook Research Institute) for scanning the stained slides, and to Dr E McVeigh of John Hopkins University, Baltimore (USA) for the DW-MRI pulse sequence. This work was financially supported by the Canadian Institutes of Health Research (grant number MOP93531).

References

Amado L C *et al* 2004 Accurate and objective infarct sizing by contrast-enhanced magnetic resonance imaging in a canine myocardial infarction model *J. Am. College Cardiol.* **44** 2383–9

Arenal A, Glez-Torrecilla E, Ortiz M, Villacastín J, Fdez-Portales J, Sousa E, del Castillo S, Perez de Isla L, Jimenez J and Almendral J 2003 Ablation of electrograms with an isolated, delayed component as treatment of unmappable monomorphic ventricular tachycardias in patients with structural heart disease *J. Am. Coll. Cardiol.* **41** 81–92

Ashikaga H *et al* 2007 Magnetic resonance-based anatomical analysis of scar-related ventricular tachycardia: implications for catheter ablation *Circ. Res.* **101** 939–47

Axel L 1998 Physics and technology of cardiovascular MR imaging *Cardiol. Clin.* **16** 125–33

Axel L 2002 Biomechanical dynamics of the heart with MRI *Annu. Rev. Biomed. Eng.* **4** 321–47

Axel L 2009 MRI of the microarchitecture of myocardial infarction: are we seeing new kinds of structures? *Circ. Cardiovasc. Imaging* **2** 169–70

Azevedo C F, NIgri M, Higuchi M L, Pomerantzeff P M, Spina G S, Sampaio R O, Tarasoutchi F, Grinberg M and Rochitte C E 2010 Prognostic significance of myocardial fibrosis quantification by histopathology and MRI in patients with severe aortic valve disease *J. Am. College Cardiol.* **56** 278–87

Bello D, Fieno D S, Kim R J, Pereles F S, Passman R, Song G, Kadish A H and Goldberger J J 2005 Infarct morphology identifies patients with substrate for sustained ventricular tachycardia *J. Am. College Cardiol.* **45** 1104–8

Bland J M and Altman D G 1986 Statistical methods for assessing agreement between two methods of clinical measurement *Lancet* **1** 307–10

Breton E, Kim D, Chung S and Axel L 2011 Quantitative contrast-enhanced first-pass cardiac perfusion MRI at 3 Tesla with accurate arterial input function and myocardial wall enhancement *J. Magn. Reson. Imaging* **34** 676–84

Chan J, Khafagi F, Young A A, Cowan B R, Thompson C and Marwick T H 2008 Impact of coronary revascularization and transmural extent of scar on regional left ventricular remodelling *Eur. Heart J.* **29** 1608–17

Cochet H *et al* 2013 Integration of merged delayed-enhanced MRI and multi-detector CT for the guidance of ventricular tachycardia ablation: a pilot study *J. Cardiovasc. Electrophysiol.* **24** 419–26

Codreanu A *et al* 2008 Electroanatomic characterization of post-infarct scars comparison with 3-dimensional myocardial scar reconstruction based on magnetic resonance imaging *J. Am. College Cardiol.* **52** 839–42

De Bakker J M *et al* 1990 Ventricular tachycardia in the infarcted, Langendorff-perfused human heart: role of the arrangement of surviving cardiac fibers *J. Am. College Cardiol.* **15** 1594–607

Dempster A P, Laird N M and Rubin D B 1977 Maximum likelihood from incomplete data with the EM algorithm *J. R. Stat. Soc.* B **39** 1–38

Dickfeld T *et al* 2008 Integration of three-dimensional scar maps for ventricular tachycardia ablation with positron emission tomography-computed tomography *JACC Cardiovasc. Imaging* **1** 73–82

Fishnein M C, Maclean D and Maroko P R 1978 The histopathological evolution of myocardial infarction *Chest* **73** 843–9

Fomovsky G M and Holmes J W 2010 Evolution of scar structure, mechanics, and ventricular function after myocardial infarction in the rat *Am. J. Physiol. Heart Circ. Physiol.* **298** H221–8

Gardner P I, Ursell P C, Fenoglio J J Jr and Wit A L 1985 Electrophysiologic and anatomic basis for fractionated electrograms recorded from healed myocardial infarcts *Circulation* **72** 96–611

Ghugre N R, Ramanan V, Pop M, Yang Y, Barry J, Qiang B, Connelly K, Dick A and Wright G A 2011 Quantitative tracking of edema, haemorrhage and microvascular obstruction after acute myocardial infarction by MRI *Magn. Reson. Med.* **66** 1129–41

Hasti T, Tibshirani R and Friedman J 2001 *The EM algorithm The Elements of Statistical Learning* (New York: Springer) pp 236–43 chapter 8.5

Helm P, Tseng H, Younes L, McVeigh E R and Winslow R 2005 *Ex vivo* 3D diffusion tensor imaging and quantification of cardiac laminar structure *Magn. Reson. Med.* **54** 850

Hennemuth A, Friman O, Huellebrand M and Peitgen H-O 2013 Mixture-model-based segmentation of myocardial delayed enhancement MRI *Statistical Atlases and Computational Models of the Heart. Imaging and Modelling Challenges: Third International Workshop, STACOM 2012* (*Lecture Notes in Computer Science* vol 7746) (New York: Springer) pp 87–96

Holmes J W, Yamashita H, Waldman L K and Covell J W 1994 Scar remodelling and transmural deformation after infarction in the pig *Circulation* **90** 411–20

Hsu E W, Buckley D L, Bui J D, Blackband S J and Forder J R 2001 Two-component diffusion tensor MRI of isolated perfused hearts *Magn. Reson. Med.* **45** 1039–45

Jansen J *et al* 2012 HVM reduced Cx43 expression triggers increased fibrosis due to enhanced fibroblast activity *Circ. Arrhythmias Electrophysiol.* **5** 380–91

Jiang H, van Zijl P C M, Kim J, Pearlson G D and Susumu M S 2006 Dti Studio resource program for diffusion tensor computation and fibre bundle tracking *Comput. Methods Programs Biomed.* **81** I06–16

Kawara T *et al* 2001 Activation delay after premature stimulation in chronically diseased myocardium relates to architecture of interstitial fibrosis *Circulation* **104** 3069–75

Kim R J *et al* 1999 Relationship of MRI delayed contrast enhancement to irreversible injury, infarct age, and contractile function *Circulation* **100** 1992–2002

Le Bihan D 1991 Molecular diffusion nuclear magnetic resonance imaging *Magn. Reson. Q.* **7** 1–30

Le Bihan D 2007 The 'wet mind': water and functional neuroimaging *Phys. Med. Biol.* **52** R57

Le Bihan D and Van Zijl P 2002 From the diffusion coefficient to the diffusion tensor *NMR Biomed.* **15** 431–4

Lima J A, Judd R M, Bazille A, Schulman S P, Atalar E and Zerhouni E A 1995 Regional heterogeneity of human myocardial infarcts demonstrated by contrast-enhanced MRI. Potential mechanisms *Circulation* **92** 1117–25

Lu Y, Nguyen T D, Codella N C, Weinsaft J, Leman B B and Wang Y 2010 Myocardial infarction segmentation by GMM clustering method with free-breathing 3D navigator-gated DE-MRI *Proc. Annu. ISMRM Meet. (Stockholm, Sweden)* abstract, p 3724

Mahrholdt H *et al* 2002 Reproducibility of chronic infarct size measurement by contrast-enhanced magnetic resonance imaging *Circulation* **106** 2322–7

Marckmann P *et al* 2006 Nephrogenic systemic fibrosis: suspected etiological role of gadodiamide used for contrast enhanced MRI *J. Am. Soc. Nephrol.* **17** 2359–62

Matiello J, Basser P J and Le Bihan D 1997 The *b* matrix in diffusion tensor echo-planar imaging *Magn. Reson. Med.* **37** 292–300

McCormick R J, Musch T I, Bergman B C and Thomas P D 1994 Regional differences in LV collagen accumulation and mature crosslinking after myocardial infarction in rats *Am. J. Physiol.* **266** H354–9

McCormick R J and Thomas P D 1998 Collagen crosslinking in the heart: relationship with development and function *Basic Appl. Myol.* **8** 143–50

Mekkaoui C, Huang S, Dai G, Reese T G, Jackowski M P and Sosnovik D 2011 *In vivo* characterization of myocardial microstructure in normal and infarcted hearts using the supertoroidal model *Proc. 19th ISMRM Conf. (Montreal)* p 281

Nakahara S *et al* 2011 Characterization of myocardial scars: electrophysiological imaging correlates in a porcine infarct model *Heart Rhythm* **8** 1060–7

Pop M *et al* 2012 Construction of 3D MRI-based computer models of pathologic hearts, augmented with histology and optical imaging to characterize the action potential propagation *Med. Image Anal.* **16** 505–23

Press W H, Teukolsky S A, Vetterling W T and Flanery B P 2007 Gaussian mixture models and k-means clustering *Numerical Recipes: The Art of Scientific Computing* (New York: Cambridge University Press) section 16.1

Ramani K, Judd R M, Holly T A, Parrish T B, Rigolin V H, Parker M A, Callahan C, Fitzgerald S W, Bonow R O and Klocke F J 1998 Contrast magnetic resonance imaging in the assessment of myocardial viability in patients with stable coronary artery disease and left ventricular dysfunction *Circulation* **98** 2687–94

Rehwald W G, Fieno D S, Chen E L, Kim R J and Judd R M 2002 Myocardial magnetic resonance imaging contrast agent concentrations after reversible and irreversible ischemic injury *Circulation* **105** 224–9

Roes S D *et al* 2009 Infarct tissue heterogeneity assessed with contrast-enhanced MRI predicts spontaneous ventricular arrhythmia in patients with ischemic cardiomyopathy and implantable cardioverter-defibrillator *Circ. Cardiovasc. Imaging* **2** 183–90

Rouillard A D and Holmes J W 2012 Mechanical regulation of fibroblast migration and collagen remodelling in healing myocardial infarcts *J. Physiol.* **18** 4585–602

Sandrasegaran K, Akisik F M, Lin C, Tahir B, Rajan J, Saxena R and Aisen A M 2009 Value of diffusion-weighted MRI for assessing liver fibrosis and cirrhosis *Am. J. Roentgenol.* **193** 1556–60

Schelbert E B, Hsu L Y, Anderson S A, Mohanty B D, Karim S M, Kellman P, Aletras A H and Arai A E 2010 Late gadolinium-enhancement cardiac magnetic resonance identifies postinfarction myocardial fibrosis and the border zone at the near cellular level in *ex vivo* rat heart *Circ. Cardiovasc. Imaging* **3** 743–52

Schuleri K H, Centola M, Kristine S, Evers K, Zvimam A, Evers R, Lima J A C and Lardo A C 2012 Cardio-vascular MR characterization of peri-infarct zone following infarction *J. Cardiovasc. Magn. Reson.* **14** 24

Shepherd T M, Thelwall P E, Stanisz G J and Blackband S J 2009 Aldehyde fixative solutions alter the water relaxation and diffusion properties of nervous tissue *Magn. Reson. Med.* **62** 26–34

Sotak 2002 The role of diffusion tensor imaging in the evaluation of ischemic brain injury—a review *NMR Biomed.* **5** 561–9

Stejskal E O and Tanner I E 1965 Spin diffusion measurements: spin echoes in the presence of time-dependent field gradient *J. Chem. Phys.* **42** 288–92

Stevenson W G 2009 Ventricular scars and VT tachycardia *Trans. Am. Clin. Assoc.* **120** 403–12

Stevenson W G *et al* 2008 Irrigated radiofrequency catheter ablation guided by electro-anatomic mapping for recurrent ventricular tachycardia after myocardial infarction: the multicenter thermocool ventricular tachycardia ablation trial *Circulation* **118** 2773–82

Sun Y and Weber K T 2005 Animal models of cardiac fibrosis *Methods Mol. Med.* **117** 273–90

Swynghedauw B 1999 Molecular mechanisms of myocardial remodeling *Physiol. Rev.* **79** 215

Taylor D G and Bushell M C 1985 The spatial mapping of translational diffusion coefficients by the NMR imaging technique *Phys. Med. Biol.* **30** 345–9

Thomas D L, Lythgoe M F, Pell G S, Calamante F and Ordidge R J 2000 The measurement of diffusion and perfusion in biological systems using magnetic resonance imaging *Phys. Med. Biol.* **45** R97

Tian J *et al* 2010 Three-dimensional contrast-enhanced multidetector CT for anatomic, dynamic, and perfusion characterization of abnormal myocardium to guide ventricular tachycardia ablations *Circ. Arrhythm Electrophysiol.* **3** 496–504

Ursell P C, Gardner P I, Albala A, Fenoglio J J Jr and Wit A L 1985 Structural and electrophysiological changes in the epicardial border zone of canine myocardial infarcts during infarct healing *Circ. Res.* **56** 436–51

Van der Voorn J P, Pouwels P J W, Powers J M, Kamphorst W, Martin J J, Troost D, Spreeuwenberg M D, Barkhof F and van der Knaap M S 2011 Correlating quantitative MRI with histopathology in x-linked adrenoeukodystrophy *Am. J. Neuroradiol.* **32** 481–9

Whittaker P, Boughner D R and Kloner R A 1991 Role of collagen in acute myocardial infarct expansion *Circulation* **84** 2123–34

Wijnmaalen A P *et al* 2011 Head-to-head comparison of contrast-enhanced magnetic resonance imaging and electroanatomical voltage mapping to assess post-infarct scar characteristics in patients with ventricular tachycardias: real-time image integration and reversed registration *Eur. Heart J.* **32** 104–14

Wu E X, Wu Y, Nicholls J M, Wang J, Liao S, Zhu S, Lau C P and Tse H F 2007 MR diffusion tensor imaging study of postinfarct myocardium structural remodelling in a porcine model *Magn. Reson. Med.* **58** 687–95

Wu M-T, Su M-Y M, Huang Y-L, Chiou K-R, Yang P, Pan H-B, Reese T G, Wedeen V J and Tseng W-Y I 2009 Sequential changes in myocardial microstructure in patients postmyocardial infarction by diffusion tensor cardiac MR: correlation with left ventricular structure and function *Circ. Cardiovasc. Imaging* **2** 32–40

Young A A, Crossman D J, Ruygrok P N and Cannell M B 2011 Mapping system for co-registration of cardiac MRI and *ex vivo* tissue sampling *J. Magn. Reson. Imaging* **34** 1065–71

Young A A, French B A, Yang Z, Cowan B R, Gilson W D, Berr S S, Kramer C M and Epstein F H 2006 Reperfused myocardial infarction in mice: 3D mapping of late gadolinium enhancement and strain *J. Cardiovasc. Magn. Reson.* **8** 685–92

Young A A, LeGrice I J, Young M A and Smaill B H 1998 Extended confocal microscopy of myocardial laminae and collagen network *J. Microsc.* **192** 139–50

Zipes D P 2005 Epidemiology and mechanisms of sudden cardiac death *Can. J. Cardiol.* **21** (Suppl A) 37A–40A